



HAL
open science

Thermal conductance of twisted-layer graphite nanofibers

Van-Truong Tran, Thanh-Tra Vu, Jérôme Saint-Martin, Marco Pala, Philippe Dollfus

► **To cite this version:**

Van-Truong Tran, Thanh-Tra Vu, Jérôme Saint-Martin, Marco Pala, Philippe Dollfus. Thermal conductance of twisted-layer graphite nanofibers. *Carbon*, 2023, 204, pp.601-611. 10.1016/j.carbon.2022.12.059 . hal-03995068

HAL Id: hal-03995068

<https://hal.science/hal-03995068>

Submitted on 27 Oct 2023

HAL is a multi-disciplinary open access archive for the deposit and dissemination of scientific research documents, whether they are published or not. The documents may come from teaching and research institutions in France or abroad, or from public or private research centers.

L'archive ouverte pluridisciplinaire **HAL**, est destinée au dépôt et à la diffusion de documents scientifiques de niveau recherche, publiés ou non, émanant des établissements d'enseignement et de recherche français ou étrangers, des laboratoires publics ou privés.

Thermal conductance of twisted-layer graphite nanofibers

Van-Truong Tran^{1*}, Thanh-Tra Vu^{2*}, Philippe Dollfus^{1*}, Jérôme Saint-Martin^{1*}, and Marco Pala^{1*}

¹Université Paris-Saclay, CNRS, Centre de Nanosciences et de Nanotechnologies, 91120, Palaiseau, France.

²Department of Physics, School of Education, Can Tho University, Can Tho, Vietnam

Abstract

We study the thermal transport properties of twisted-layer graphite nanofibers. We show that in the presence of a twisted layer, the phonon thermal conductance of a graphite nanofiber of rectangular cross-section varies remarkably with the twisted angle and can reach minimum values either at two critical angles θ_1 and θ_2 that conform to the rule $\theta_1 + \theta_2 = 180^\circ$ or exactly at the angle $\theta = 90^\circ$. A reduction of roughly 50% of the phonon thermal conductance can be achieved in some structures. We unveil that the twisting effect mainly influences the optical modes, leaving almost unaltered the acoustic ones. The effect is also visible in the higher and more numerous van Hove singularities of the phonon density of states. We also point out that the behavior of the thermal conductance with the twist angle is associated with and dominated by the alteration in the overlap area between the twisted and non-twisted layers. The finite-size effect is demonstrated to play an essential role in defining the critical angles at the local minima, where these angles are dependent on the size of the investigated nanofibers, in particular in the proportion between the widths of zigzag and armchair edges. We also analyze the behavior of circular nanofibers where the correlation between the overlap area and the thermal conductance is much smaller.

1. Introduction

The twisting effect in bilayer graphene results in novel physics when compared to non-twisted structures[1–5]. In particular, exceptional electronic characteristics with superconducting states have recently been reported at the magic angle of around 1.1 degree[6]. Numerous researches on the electronic properties of twisted structures in bilayer and few-layer graphene systems[7–

*E-mails: vantruongtran.nanophys@gmail.com (V-T. Tran), vttra@ctu.edu.vn (T-T. Vu), philippe.dollfus@c2n.upsaclay.fr (P. Dollfus), jerome.saint-martin@c2n.upsaclay.fr (J. Saint-Martin), marco.pala@c2n.upsaclay.fr (M. Pala)

12] as well as other 2D materials like black phosphorus[13] have been motivated by this fascinating physics. It also creates a new field of electronics known as “twistronics” and opens up a vast range of opportunities of exploiting the twisting effect[14].

The findings on the electronic properties of the twisted graphene layers have also inspired some studies on the impact of this effect on their thermal properties. However, the number of works dedicated to the thermal properties of twisted graphene structures is still modest[15,16].

Regarding in-plane phonon characteristics, in 2013 Cocemasov *et al.*[17] studied phonon properties in twisted bilayer graphene, focusing more on AA-stacking structures. They showed that the twisting effect induces the largest impact on out-of-plane acoustic (ZA) modes in the phonon bands of the bilayer structures. Even so, the impact is still noticeable on optical and other acoustic modes[17], and also in AB-stacking bilayer structures[18]. Interestingly, both experiments and molecular dynamic (MD) simulations showed in-plane phonon conductivity reaching the minimum near the twist angle equal to 15° or 45° and a local maximum at 30° [16,19], demonstrating tunable features of thermal transport in twisted bilayer and multiple layer graphene systems.

Although for few-layer graphene structures, in-plane phonon transport is more important, thermal transport across the layers was also assessed. By using MD simulations, Wang *et al.*[15], and Nie *et al.*[16] pointed out that the perpendicular thermal conductivity in bilayer and few-layer graphene structures could reach a minimum at the twist angle of about 30° , in contrast to the in-plane thermal transport[16,19]. Such results were essentially observed in 2D structures, i.e., in structures where layers are assumed to expand infinitely, while the investigation of thermal properties for twisted structures of finite size is still lacking.

It is worth noting that the finite-size effect in structures such as quasi-1D graphene ribbons offers extended physical properties compared to those of 2D structures. For instance, the observed finite-bandgap in these structures as well as novel physics from the edge-type terminations[20] make them suitable for a variety of electronic applications[20–22]. Thus one could expect that the combination of both twisting and finite-size effects might result in novel phenomena in finite-size multiple-layer graphene structures compared to what has been observed in 2D counterparts. Such studies still need to be conducted at both fundamental and practical levels.

Graphite nanofibers (GNFs) have recently attracted great attention for their extremely high thermoelectric capacity[23]. Such structures can be also considered as relevant for exploring

the combined twisting and finite-size effects, due to the high probability to find twisted layers in these systems and to the fact that each basic cell has finite size with borders made of a mixture of zigzag and armchair edges. Therefore, in this work, we focus on the impact of the twisting effect on the thermal transport in twisted-layer graphite nanofibers. Our study aims at providing a fundamental understanding of the twisting effect in finite-size structures. ~~but also intends to reveal how such an effect could play a role in applications of graphite nanofibers.~~

The paper is organized as follows. In Sec. 2, we describe in detail the studied systems and then briefly present the methodology based on the efficient Force Constant (FC) model and the Non-Equilibrium Green's Functions (NEGF) formalism. Section 3 discusses the obtained results, more precisely in Sec. 3.1, we investigate the variation of phonon thermal conductance as a function of the twist angle in GNFs of rectangular cross-section, and in Sec. 3.2, we analyze the role of the finite-size effect. In Sec. 3.3 we discuss the case of GNFs with circular cross-section, while Sec. 4 is devoted to conclusions.

2. Studied system and methodology

2.1. Studied system

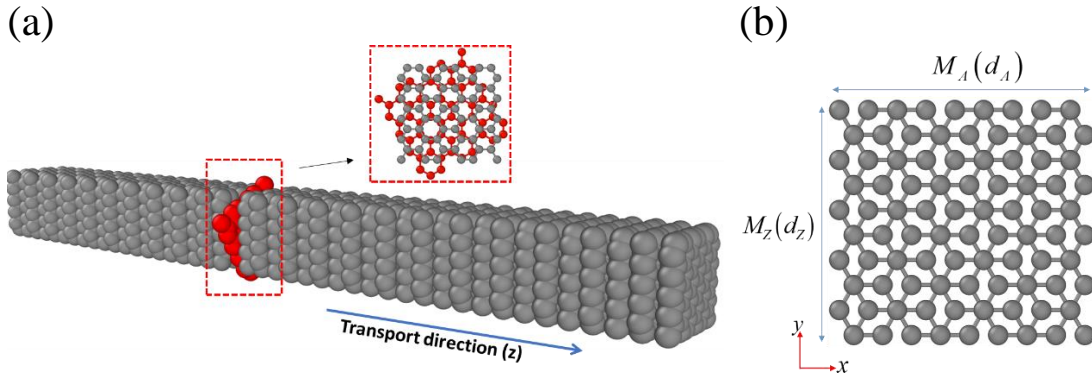


Figure 1. (a) Sketch of a nanodevice made of “platelet” graphite nanofibers with rectangular cross-section and containing a twisted layer marked in red. (b) The atomistic view of a basic cell containing $2M_A \times M_Z$ atoms. The illustration is for the nanofibers with $M_A = 6$ ($d_A \approx 1.207$ nm), $M_Z = 10$ ($d_Z \approx 1.107$ nm).

Figure 1(a) illustrates the studied device composed of a GNF of rectangular cross-section in the presence of a twisted layer that is marked in red. In Sec. 3.3 we will also examine the case of nearly circular GNFs (not schematized here). The transport direction is along the c-axis, perpendicular to the graphite layers. It is worth mentioning that among several types of GNFs,

this kind of structure is classified as “platelet” graphite nanofibers[24,25]. For the sake of convenience, the c-axis is identical to the z-axis and the rotation is performed around this axis. In Fig. 1(b), a basic cell containing two sub-layers is shown. The diameter of the fiber is characterized by the number of slices in each sub-layer along the armchair and zigzag edges, M_A and M_Z , respectively. The widths d_A and d_Z of the GNF along armchair and zigzag edges can be determined as $d_A = (3M_A - 2) \times a_0 / 2 + a_0 / 2$ and $d_Z = (M_Z - 1) \times \sqrt{3} / 2 \times a_0$, where $a_0 \approx 0.142$ nm is the distance between the two nearest in-plane carbon atoms.

In this work, we consider nanofibers of diameter ranging from sub-nano to more than 2 nm. We remark that such small diameters are experimentally reachable thanks to the recent developments of the CVD technique in growing carbon nanostructures[26].

2.2. Methodology

The basic cell of studied graphite nanofibers contains hundreds of atoms, which, with a view to phonon transport analysis in defected twisted structures, is highly challenging for *ab-initio* calculations. We therefore employed the Force Constant (FC) approximation as an efficient approach to construct dynamical matrices, and we combined it with the Non-Equilibrium Green’s Functions (NEGF) formalism for simulating the phonon transport properties.

Force Constant model

An FC model containing both in-plane and van der Waals (vdW) interactions was employed. It accurately reproduces the phonon dispersion of both graphene layers and graphite along the c-axis obtained from *ab-initio* methods as well as experimental measurements [18,27]. The secular equation for phonons deriving from Newton’s second law reads [28,29]:

$$\omega^2 U = D U, \quad (1)$$

where U is the column matrix containing the amplitude vectors of vibration of all lattice sites, ω is the angular frequency, and D is the Dynamical matrix that is calculated as [28]:

$$D = [D_{3 \times 3}^{ij}] = \begin{cases} -\frac{K_{ij}}{\sqrt{M_i M_j}} & \text{for } j \neq i \\ \sum_{j \neq i} \frac{K_{ij}}{M_i} & \text{for } j = i \end{cases}, \quad (2)$$

where M_i is the mass of the i -th atom and takes the value of 1.994×10^{-26} kg for each carbon atom. K_{ij} is the 3×3 coupling tensor between the i -th and j -th atoms and is defined depending on whether it is in-plane or inter-plane interaction, i.e.,

(i) For in-plane interactions, K_{ij} was defined by a unitary in-plane rotation [28,29]

$$K_{ij} = U^{-1}(\theta_{ij}) K_{ij}^0 U(\theta_{ij}), \quad (3)$$

in which $U(\theta_{ij})$ is the rotation matrix [29] defined by

$$U(\theta_{ij}) = \begin{bmatrix} \cos(\theta_{ij}) & \sin(\theta_{ij}) & 0 \\ -\sin(\theta_{ij}) & \cos(\theta_{ij}) & 0 \\ 0 & 0 & 1 \end{bmatrix}. \quad (4)$$

The angle θ_{ij} is the anticlockwise rotating angle formed between the positive direction of the x -axis and the vector from the i -th atom to the j -th atom. K_{ij}^0 is the force constant tensor given by:

$$K_{ij}^0 = \begin{pmatrix} \Phi_r & 0 & 0 \\ 0 & \Phi_{t_i} & 0 \\ 0 & 0 & \Phi_{t_o} \end{pmatrix}, \quad (5)$$

where Φ_r , Φ_{t_i} and Φ_{t_o} are the force constant coupling parameters in the radial, transverse in-plane, and out-plane directions, respectively. In this work, these in-plane force constant parameters were considered up to four nearest neighbor interactions, and therefore twelve parameters are needed for in-plane couplings. The values of these parameters were taken from Wirtz's work [27].

(ii) For interactions between layers (vdW interactions), we employed the spherically symmetric interatomic potential model, in which each component of the coupling tensor K_{ij} is defined by: [18]

$$(K_{ij})_{kk'} = \delta(r^{ij}) \frac{r_k^{ij} r_{k'}^{ij}}{(r^{ij})^2} \quad (6)$$

where k, k' is one of the x, y, z components. r^{ij} is the vector from the i -th to the j -th atom. $\delta(r^{ij})$ is the decaying component $\delta(r^{ij}) = A \cdot \exp(-r^{ij}/B)$ with empirical parameters $A = 573.76$ N/m, $B = 0.05$ nm. It is worth mentioning that the minus sign “-” is not present in equation (6) as in ref. [18] because this sign has been already included in equation (2). In practice, to find the best fit between the FC model and the experimental data for bulk graphite, we chose the distance between two graphite layers equal to 0.328 nm. In addition, to simplify the computation, a cut-off of 1 nm in real space was applied for r^{ij} in Eq. (6).

Green's function formalism for transport study

To investigate the phonon transport properties, we employed the NEGF technique which is highly relevant to study transport in nanostructures, including defects [30]. Within this technique, all considered structures are divided into three parts: the left and right leads and the device (central) region. The leads were considered as semi-infinite periodic regions. The device region contains studied defects and has the length characterized by the number of basic cells N_A .

The retarded Green's function for phonons can be written as:

$$G = [\omega^2 + i\eta - D_D - \Sigma_L^s - \Sigma_R^s]^{-1}, \quad (7)$$

where η is a positive infinitesimal number, D_D is the dynamical matrix of the device (scattering region), and

$$\begin{aligned} \Sigma_L^s &= D_{DL} G_{L(L)}^0 D_{LD} \\ \Sigma_R^s &= D_{DR} G_{R(R)}^0 D_{RD} \end{aligned} \quad (8)$$

are the surface self-energies representing the contribution of the left and right contacts, respectively, being $G_{L(R)}^0$ the surface Green's function of the isolated left (right) contact. The self-energies were computed using the Sancho-Rubio iterative technique[31].

To compute efficiently the phonon transmission, the recursive technique [32] was employed to handle the size of the device Hamiltonian in the Green's function calculation. Phonon transmission was then computed as [28,30]:

$$T_p = \text{Trace} \left\{ \Gamma_{L(R)}^s \left[i(G_{11} - G_{11}^\dagger) - G_{11} \Gamma_{L(R)}^s G_{11}^\dagger \right] \right\}, \quad (9)$$

where $\Gamma_{L(R)}^s = i(\Sigma_{L(R)}^s - \Sigma_{L(R)}^{s\dagger})$ is the surface injection rate at the left (right) contact.

The phonon thermal conductance K_p was computed by [28]

$$K_p = \frac{k_b}{2\pi} \int_0^\infty d\omega \Gamma_p(\omega) g^p(\omega, T), \quad (10)$$

where $g^p(\omega, T) \equiv \left(\frac{\hbar\omega}{2k_B T} \right)^2 / \sinh^2 \left(\frac{\hbar\omega}{2k_B T} \right)$.

3. Results and discussions

In this section, we first examine the variation of the phonon thermal conductance as a function of the twist angle. Then, we analyze the role of the finite-size effect in defining the characteristics of such a variation.

3.1. Crucial angles at minimum thermal conductance

We investigate the dependence of the thermal conductance in nanofibers of rectangular cross-section on the twist angle of a single twisted layer within the system.

Figure 2(a) shows the phonon thermal conductance at room temperature as a function of the twist angle of the GNF with the size $M_A = 6$ ($d_A \approx 1.207$ nm), $M_Z = 10$ ($d_Z \approx 1.107$ nm). The results of three cases with different positions of the twisted layer and different device lengths are displayed. The position of the twisted layer is characterized by the two indices $[n_{cell}, n_{layer}]$, where n_{cell} indicates the cell number in the device region that contains the twisted layer, and n_{layer} is either 1 or 2 to indicate which of the two layers in the basic cell is twisted.

When the twisted angle is tuned from 0 to 180°, at the first glance, it can be seen that the phonon thermal conductance varies remarkably: the curve forms two valleys around 45° and 135°, respectively, together with a peak located around the twist angle of 90°. It is worth mentioning that with twist angles ranging from 180° to 360°, the results (not shown) lead to a symmetrical curve, which makes sense since rotations from 180° to 360° are equivalent to those from 0 to -180°, that are equivalent to those from 0 to 180°. On the other hand, there is not a perfect

symmetry with respect to the 90° as the stacking is different on the two sides of this angle. For example, the non-twisted structure and the structure twisted with an angle of 180° do not have the same conductance as they exhibit AB and AA stacking, respectively.

It can be observed that although the minimum thermal conductance depends on the position and the length of the device, the twist angle corresponding to the minimum thermal conductance remains unchanged, i.e., at 45° and 135° for the studied structure. In addition, these two angles satisfy the rule

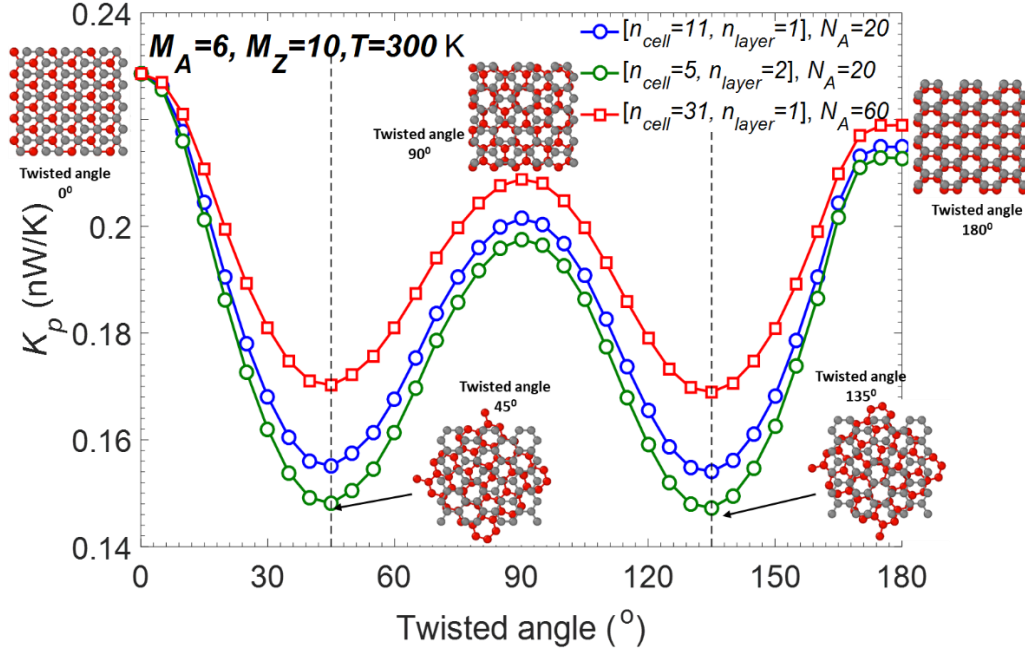
$$\theta_1 + \theta_2 = 180^\circ. \quad (11)$$

The thermal conductance of twisted structures is reduced remarkably compared to that of the non-twisted one. For example, in the case of the green curve, at 45° and 135° , K_p reaches a minimum at the values of 0.148 nW/K and 0.147 nW/K , respectively. Compared to the conductance of 0.229 nW/K for the non-twisted structure, it is a reduction of about 35%. Such a reduction in the thermal conductance is very appealing for thermoelectric applications since it can boost the thermoelectric figure of merit ZT .

The phonon thermal conductance as a function of the twist angle is given in Fig. 2(b) at temperatures other than room temperature. It shows clearly that the variation at different temperatures is similar. Interestingly, the twist angles at the minimum thermal conductance are likewise unaltered.

The results depicted in Figs. 2(a) and 2(b) thus show that the two twisted angles at the minimum conductance are crucial and independent of the position of the twisted layer as well as of temperatures.

(a)



(b)

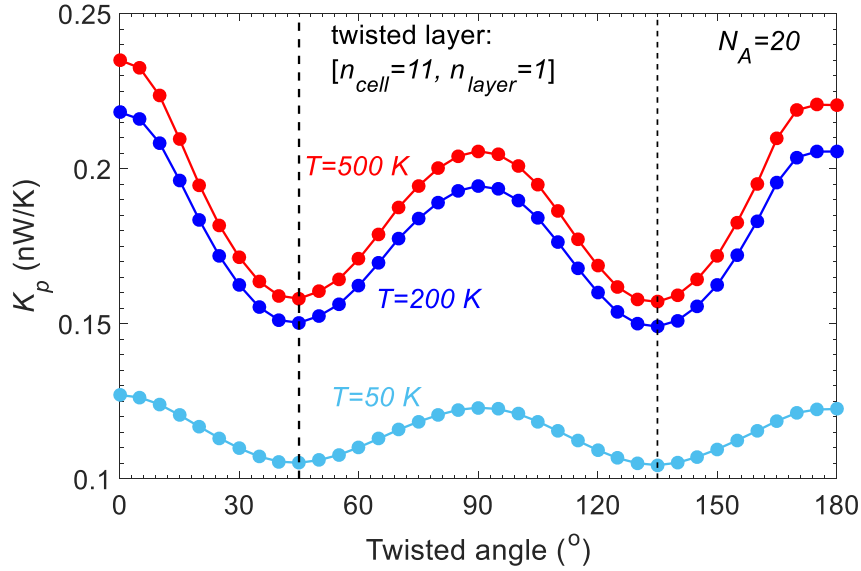


Figure 2. (a) Thermal conductivity at room temperature is plotted as a function of twisted angle with different positions of the twisted layer and different device length N_A . (b) Thermal conductivity as a function of the twisted angle at different temperatures. In all cases, the same size nanofiber was considered $M_A = 6$, $M_Z = 10$.

To explore the underlying physics of the variation in phonon thermal conductivity as a function of the twist angle, it is relevant to look at the phonon bands of the periodic structures even though defects do not appear periodically in the systems. For twisted structures, we will consider periodic structures with a twisted layer in a basic cell. The phonon bands can be defined from the eigenvalues of the equation which is simplified from Eq. (1) to the equation for a single unit cell:

$$dU = \omega^2 U, \quad (12)$$

where d is the dynamic matrix defined as

$$d = D_{00} + \sum_{\alpha \neq 0} D_{0\alpha} \cdot e^{i\vec{k} \cdot (\vec{R}_\alpha - \vec{R}_0)}, \quad (13)$$

where D_{00} is the dynamical matrix of the cell 0 and $D_{0\alpha}$ is the dynamical matrix describing the coupling between the cells 0 and α .

The influence of the twisting effect on the phonon modes can be confirmed using the phonon density of states (DOS), which is very sensitive to changes in the phonon bands. We calculated the phonon DOS by using the Gaussian smearing of the Dirac delta function [33], i.e.,

$$DOS(\omega) = \sum_n \sum_{\vec{k} \in BZ} \delta(\omega - \omega_n(\vec{k})) \approx \sum_n \sum_{\vec{k} \in BZ} \frac{1}{\eta\sqrt{\pi}} e^{-\frac{(\omega - \omega_n(\vec{k}))^2}{\eta^2}}, \quad (14)$$

where n is the phonon band index, \vec{k} is a wave vector in the first Brillouin zone (BZ), η is a small positive number, and $\omega_n(\vec{k})$ is the frequency of the n -th phonon mode at the wave vector \vec{k} , which is calculated from equation (12). Equation (14) is a generic formula that can also be used to calculate the phonon DOS for 2D and 3D structures.

Phonon bands are shown in Fig. 3(a) for three cases of the twisted angle. As can be seen, when the structure is twisted, mini-gaps are slightly widened between optical bands and, in parallel, these bands are flattened. These effects seem stronger when increasing the twist angle. However, it appears that the acoustic modes are only marginally affected by the distortion of the structure. Such an outcome reveals that the effect of the twisted layer is similar to that of isotope doping observed in in-plane graphene ribbons[34].

The DOS depicted in Fig. 3(b) makes this insight more obvious. They present van Hove singularities that are particularly noticeable around nearly flat bands. The DOS of twisted structures (color lines) shows more numerous as well as higher peaks compared to that of the non-twisted structure (black). Also, the twisted structures present larger mini-gaps and open new mini-gaps right above 100 cm^{-1} . This effect is particularly visible in the frequency range

from 70 to 250 cm^{-1} . Below 50 cm^{-1} where acoustic modes locate, the DOS is weakly modified. These results are consistent with what has been observed with the phonon bands. The DOS obtained for the twisted angle equal to 60° was also plotted for comparison (dashed line). It appears that this DOS presents smaller changes than that obtained for 45° . That is clearly reflected around the mini-gaps and in the frequency range from 70 to 150 cm^{-1} . This outcome is coherent with the results of thermal conductance seen in Fig. 2 and suggests that the twisting seems to have the highest impact around the angle of 45° .

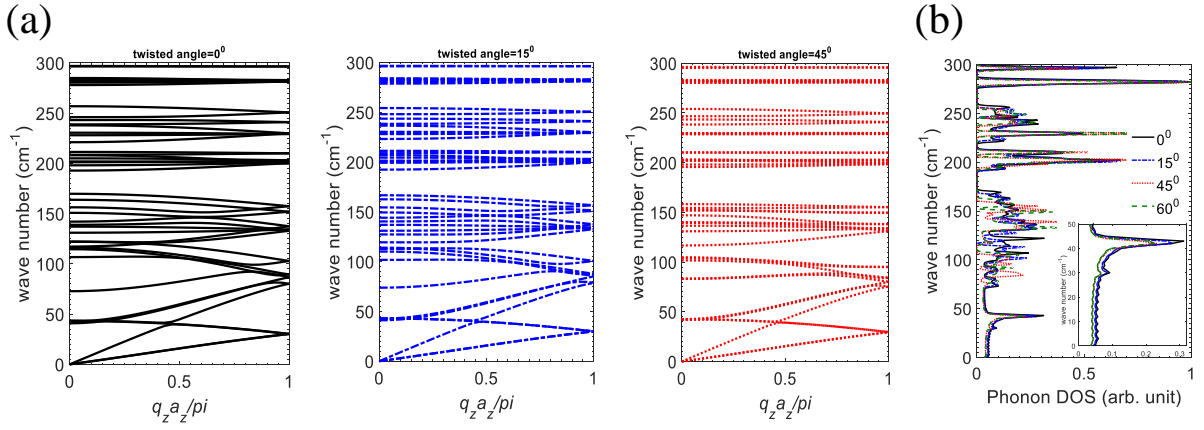


Figure 3. (a) Phonon bands of non-twisted and twisted periodic structures with an assumption that a layer in the basic cell is rotated. (b) Phonon density of states corresponding to different twisted angles. The size of the nanofiber: $M_A = 6$, $M_Z = 10$.

Although the phonon bands and the phonon DOS give some insights to interpret the transport properties, it is challenging to exploit them to monitor change at various twisted angles.

To identify the main factors involved in the variation of the thermal conductance at each twisted angle, we focus on the overlap area between the twisted and non-twisted layers, as shown in atomic structures inserted in Fig. 2(a) for different angles. At the twisted angle of 45° , the overlap area is smaller than that at 0° and 90° , which means that the variation of the phonon thermal conductance might be associated to the change of the overlap area between the twisted and non-twisted layers. To elucidate this prediction, we explored the overlap area by

considering two layers as two polygons and examined the overlap of these polygons when one is twisted. The overlap area as a function of the twisted angle is shown in Fig. 4.

Interestingly, the variation of the overlap area with the twisted angle in Fig. 4 is very similar to that of the phonon thermal conductance in Fig. 2. The two local minima are also located at 45° and 135° . Thus, the main characteristics of the curve of K_p against the twisted angle are strongly associated with the overlap area of the twisted and non-twisted layers. It is worth noting that, the overlap area at 90° is close that at 0° . However, the thermal conductance at these two angles is visibly distinct as can be seen in Fig. 2(a). This indicates that the thermal conductance of the twisted layer depends also on the relative position between atoms in the different layers, which is understandable as it defines the strength of the van der Waals interactions. However, the remarkable resemblance between the variation of the overlap area and the thermal conductance with the twist angle reveals that the overlap area between twisted and non-twisted layers in nanofibers dominates the characteristics of the change in the thermal conductance.

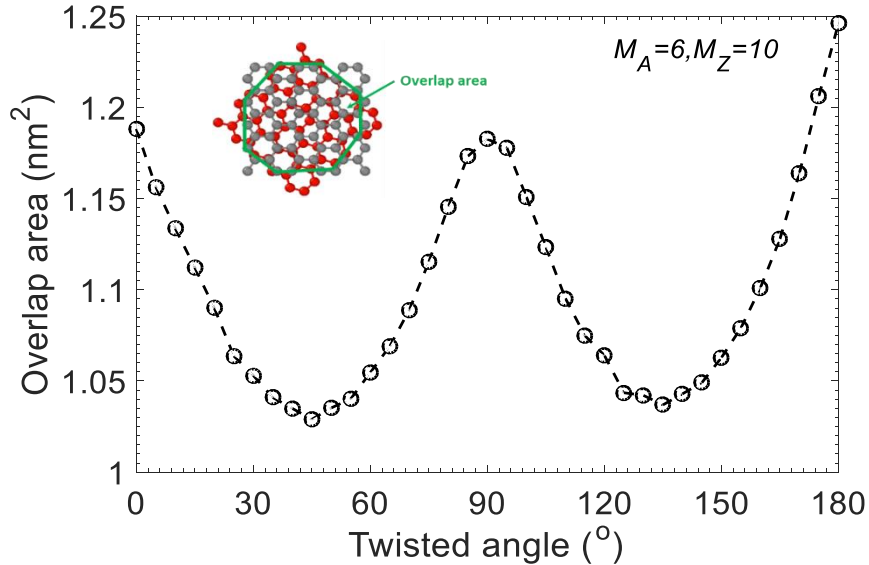


Figure 4. The overlap area of the two layers in a basic cell when one layer is twisted. Here $M_A = 6, M_Z = 10$.

3.2. Finite-size effect

In general, the size of the nanofibers, namely d_A and d_Z , determines the overlap area between the twisted and non-twisted layer. On the other hand, as demonstrated in Sec. 3.1, a correlation between the overlap area and the thermal conductance exists, thus suggesting that the crucial

angles at the minimum thermal conductance might be subjected to the finite-size effect. In this section, we, therefore, consider the variation of thermal conductance with the twist angle for nanofibers of different sizes to unveil the role of this effect.

In Fig. 5, the thermal conductance at room temperature is shown for four twisted structures of different size. Due to the strong dependence of thermal conductance on the size of the structures, to make all results clearly visible on the same graph, we normalized the obtained thermal conductance of the twisted structure to that of the non-twisted one for each structure size considered.

As can be observed, most structures exhibit a curve with two valleys at the two sides of a peak located at the twisted angle of 90° , similarly to those observed for the structure $M_A = 6, M_Z = 10$ shown in Fig. 2(a). However, the depth and the position of the valleys depend on the size of the structure. Interestingly, the curve corresponding to the structure with the size $M_A = 6, M_Z = 7$ (blue diamonds) displays a distinct pattern in relation to the twist angle, i.e., the lowest thermal conductance is precisely determined at 90° .

It is also worth noting that the largest considered structure (cyan triangles) shows a reduction of thermal conductance reaching almost 50%, which is potentially very interesting for applications such as thermoelectrics.

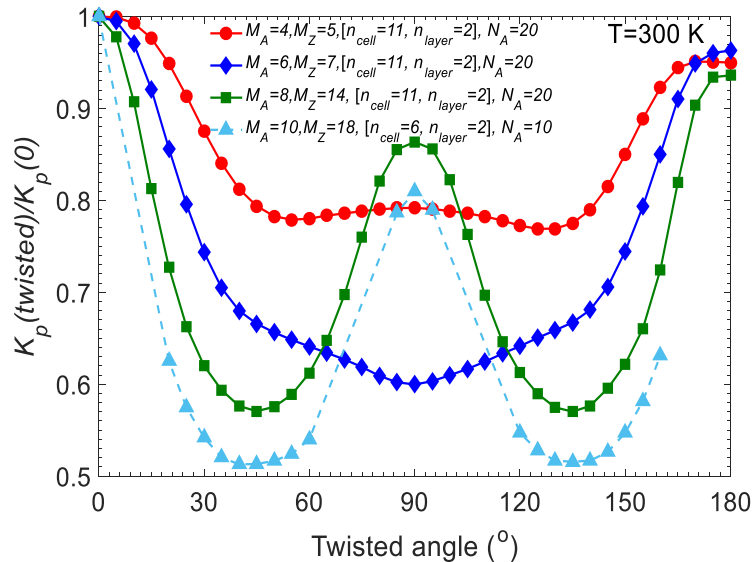


Figure 5. Phonon conductance of twisted nanofibers with different sizes normalized to that of the non-twisted structures.

To explore the finite-size effect, we first examine the critical angle at the first local minimum K_p as a function of the crossing area $S = d_A \times d_Z$. The results are shown in Fig. 6(a). It is important to note that, in all instances, Eq. (11) remains true for the two twist angles at the lowest thermal conductance, therefore an investigation at the first important angle should be sufficient.

Fig. 6(a) clearly shows that the first critical angle varies significantly with the crossing area of the nanofibers. The black lines at each data point present the error bar. To limit the computational burden, we have made calculations by changing the twist angle by steps of 5° . The error bar on each side (upper and lower) of a data point is thus 2.5° . The critical angle of about 30° of the periodic infinite cross-section multi-layer structures known from Refs. [15,16] was also added (cross symbol) for comparison.

The critical angle of the bigger structure appears to be smaller at the first look. However, the structure $M_A = 6, M_Z = 7$ (blue symbol) has an abnormal larger critical angle compared to that of the structure $M_A = 4, M_Z = 5$ (red symbol), despite having a larger crossing area. Hence, the critical angle depends also on other factors than only the crossing area.

We notice that the three largest structures considered here have a ratio $d_A/d_Z \sim 1$ with a small difference in the critical twisted angle (around 45° and 40°), while the two structures which have a higher critical angle have a parameter d_A/d_Z far from 1. To unveil the role of the ratio d_A/d_Z (we can consider also d_Z/d_A), we plot the critical angle of the first minimum conductance as a function of the ratio d_A/d_Z in Fig. 6(b). As can be observed, the dependence of the critical angle on the proportion of the edge widths presents a clearer rule than that with the crossing area. With a ratio around 1, the critical angle is close to 40° - 45° and can converge to lower values if the crossing area is larger. When this ratio is far from 1, the critical angle increases further, and can reach the value of 90° if the ratio is significantly large, i.e. above 1.6.

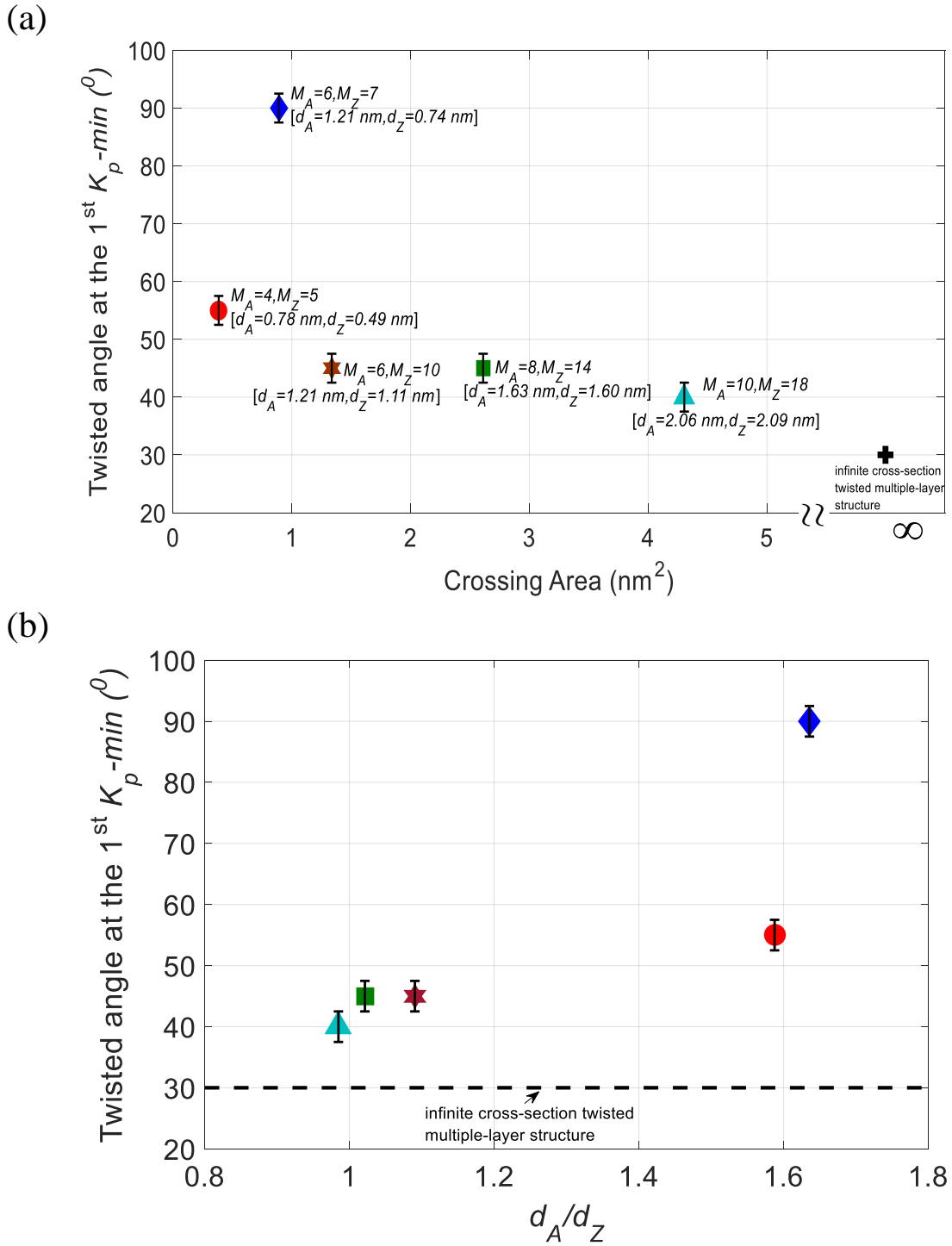


Figure 6. The crucial twist angle at the first local minimum thermal conductance of different size nanofibers is plotted as a function of (a) the crossing area $S = d_A \times d_Z$, and (b) of ratio d_A/d_Z . The cross symbol in panel (a) and the dashed line in panel (b) correspond to the result of an infinite cross-section twisted multiple-layer graphene structure [15,16].

We have seen that the three red, green, and cyan curves of thermal conductance for different structures in Fig. 5 have a twist-angle-dependence similar to that of the structure considered in

Fig. 2. We checked and observed that this behavior is also the same as that of the overlap area depicted in Fig. 4. However, the blue curve in Fig. 5 shows a distinct behavior, and it is worth checking if in this case the variation of the overlap area still agrees with that of the thermal conductance.

In Fig. 7(a), we show the thermal conductance at room temperature for two cases of different positions of the twisted layer. In both cases the minimum of conductance occurs at the same twist angle of 90° . The atomistic view around the twisted layer for some values of the twist angle is also inserted in the panel and shows that the smaller overlap area seems to be observed around 90° . To confirm this, we examined the overlap area as a function of the twist angle and plotted it in Fig. 7(b). The result of the overlap area also shows a minimum at 90° and thus reinforces the fundamental role of the overlap area in all cases of the size of graphite nanofibers.

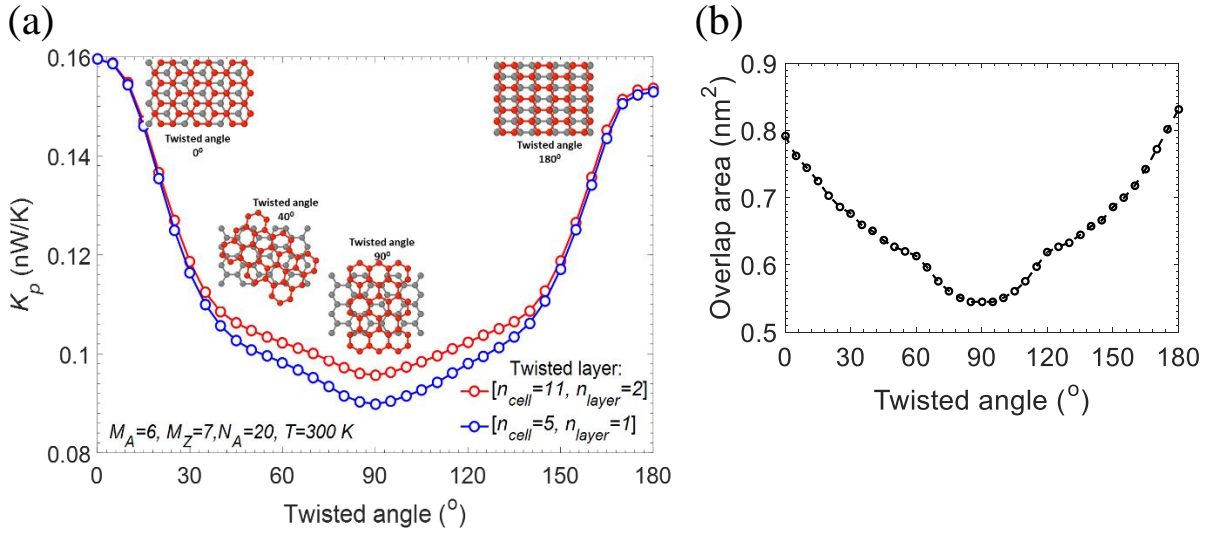


Figure 7. (a) Thermal conductance of nanofibers at 300 K with the size $M_A = 6$ ($d_A = 1.21$ nm) $M_Z = 7$ ($d_Z = 0.74$ nm) as a function of the twisted angle. (b) The overlap area of the twisted and fixed layers in a basic cell versus the twisted angle.

3.3. The case of circular graphite nanofibers

Above analyses for GNFs of rectangular cross-section have unveiled the important role of the overlap area. In the case of circular cross-sections GNFs, the overlap area should remain weakly dependent on the twisted angle. It is thus relevant to investigate the correlation between the overlap area and the change of the phonon thermal conductance in circular nanofibers.

To create a circular cross-section structure, we simply removed some atoms in the corners of the rectangular-cell structure presented in Fig. 1, so the same values of M_A and M_Z are used to determine the size of a circular structure. For the sake of convenience, we chose to remove all the atoms that are out of the circle of radius $R = \sqrt{(\min((x_{\max} - x_{\min})/2, (y_{\max} - y_{\min})/2))^2 + (a_0/2)^2} + a_0/4$.

In practice, at the atomic level, we can only obtain nearly circular cross-section structures. As a result, the two layers of a basic cell do not perfectly overlap and the overlap area still varies slightly with the twist angle. In the first row of Fig. 8, we show the variation of overlap area for three circular structures of different size. The variation of the overlap area is evaluated as $\text{Variation of overlap area} = [S_{\text{overlap}}(\text{twisted}) - S_{\text{overlap}}(\text{non-twisted})] / S_{\text{overlap}}(\text{non-twisted}) \times 100\%$. A negative value of this quantity indicates a reduction of the overlap area.

The second row of Fig. 8 shows the change in the thermal conductance for each structure.

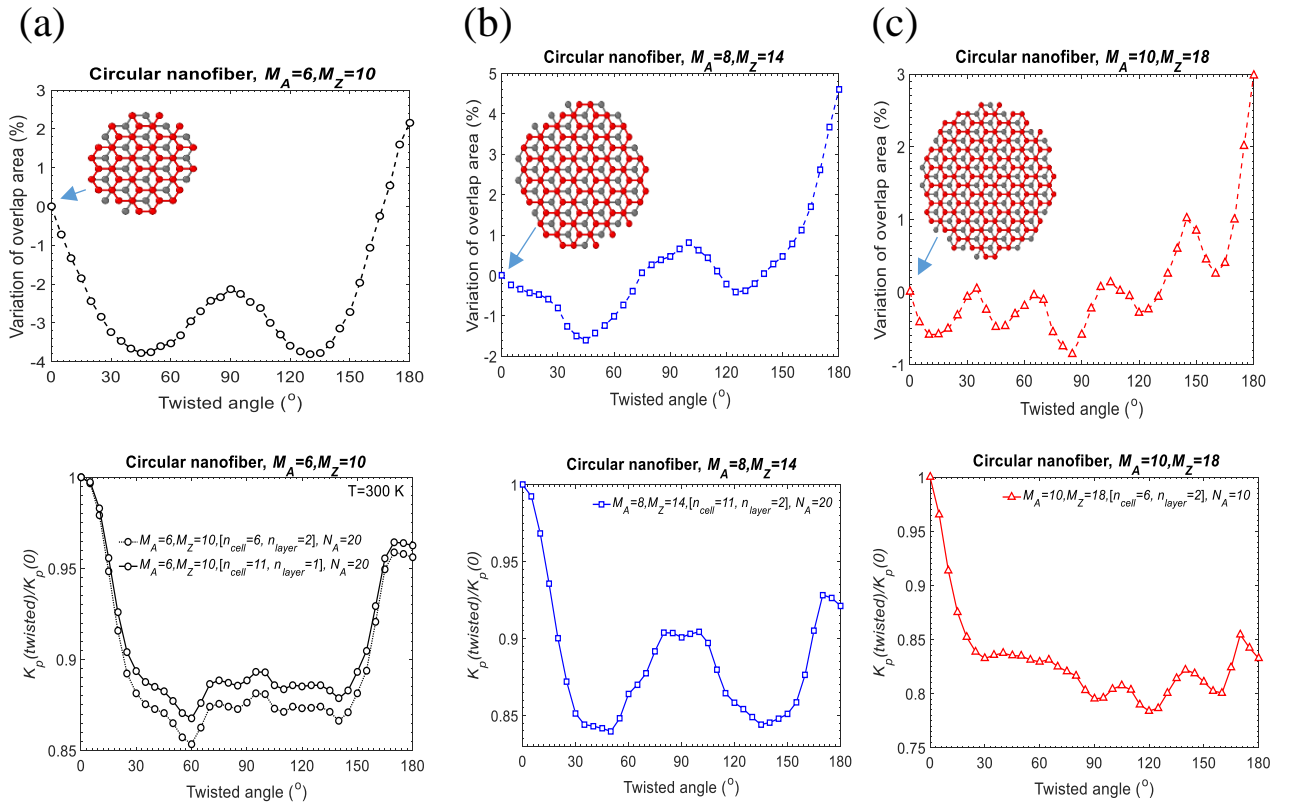


Figure 8: Variation of overlap area and thermal conductance of three different circular cross-section graphite nanofibers.

As can be observed, the thermal conductance curves in Figs. 8(a) and 8(b) exhibit some characteristics of the curves of the variation of the overlap area, however, they do not have the same form as the case of the rectangular nanofibers considered in sections 3.1 and 3.2. In

particular, the largest considered structure in Fig. 8(c) displays a remarkable difference between the variation of the overlap and the one of the thermal conductance. Thus, the role of the overlap area is weaker and even almost negligible in the case of circular nanofibers.

To understand more deeply such a discrepancy, and eventually link it to the case of the rectangular GNFs for a global conclusion, we analyzed in more detail the variation of the overlap area with the twisted angle for each structure. In the first row of Fig. 8, we can see that when the overlap reaches its minimum, the variation of the overlap does not exceed 3.8%, 1.6%, and 0.85% in Figs. 8(a), 8(b) and 8(c), respectively. Interestingly, the variation degree of the overlap seems proportional to the correlation between the overlap area and the change of the thermal conductance, i.e., the similarity between the curves of the conductance and the overlap area in Fig. 8(a) is higher due to a larger variation of the overlap, and it is almost invisible in Fig. 8(c) due to a small change of the overlap. This suggests that a strong correlation between the conductance and the overlap area in the case of the rectangular nanofibers must correspond to a significant variation degree of the overlap area in these structures. We can verify this prediction by looking at Fig. 4 and Fig. 7, or Fig. 9 below. Indeed, in these rectangular cross-section nanofibers, the change of the overlap at its minima can reach 15% and even more than 30% as can be seen in Fig. 9.

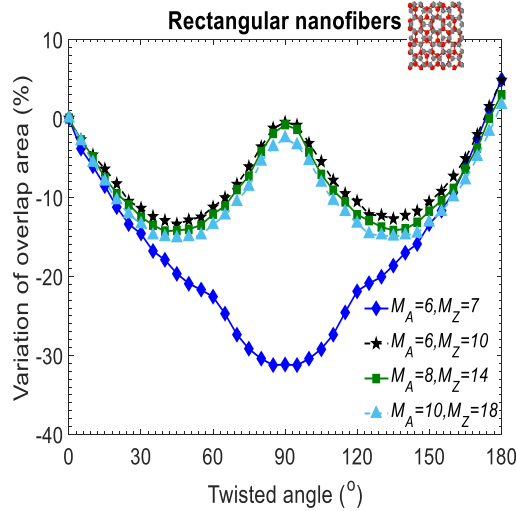


Figure 9: Variation of the overlap area of several rectangular cross-section nanofibers

Thus, we can conclude that the correlation between the overlap area and the change of the phonon thermal conductance is proportional to the variation degree of the overlap area. The overlap is a dominant factor that defines the characteristics of the variation of the thermal conductance with the twist angle in the structures where the overlap area varies significantly.

The role of the overlap area is much smaller, if not fully negligible, in circular nanofibers due to the smaller variation of this quantity.

Last but not least, it is also worth discussing the feasibility of the studied systems in the view of the experimental context. First, concerning the fabrication of carbon structures including graphene and graphite nanofibers, finite-size structures such as ribbons can be fabricated by using top-down[35] or bottom-up techniques[35]. The former approach always produces ribbons with relatively rough edges which strongly impacts the properties of the structure[35] and also cannot be used to fabricate narrow ribbons of few nm in width. The latter allows us to control ribbons in desired shapes and with smooth edges[35]. In 2015, based on the bottom-up technique, Kimouche et al.[36] grew successfully the smallest graphene ribbon with a width of 5 dimer lines (~ 0.5 nm) in an ultra-high vacuum. Since the 2000s, it has been also possible to synthesize graphite nanofibers with diameters of about 2 nm using the bottom-up technique[37–39]. Second, concerning techniques to twist layers, the control of the twist angle is now possible thanks to recent development techniques by combining wafer-scale highly-oriented monolayer growth techniques and a water-assisted transfer method[40]. On the other hand, different techniques such as using microdevice[41] or “T-type probe”[42] have been employed successfully to measure the thermal conductivity of individual nanofibers with a diameter ranging from a few tens to hundreds nm. Thus, with rapid development in experimental techniques, the thermal transport properties of graphite nanofibers considered in this work could be verified experimentally.

4. Conclusion

We have studied the phonon transport properties in twisted-layer graphite nanofibers. We demonstrated that in the presence of a twisted layer, the phonon thermal conductance of such systems varies significantly. Interestingly, we found that the thermal conductance reaches a local minimum at the two angles θ_1, θ_2 around 90° or at exactly 90° and these critical angles are independent of the position of the twisted layer and the length of the device, but it depends on the shape of the cross section.

We pointed out that the variation of the thermal conductance stems from the change of phonon modes due to the twisting effect. It was unveiled that the twisting effect impacts strongly the optical modes, in particular, in the frequency range from 70 cm^{-1} to 250 cm^{-1} , and it weakly influences the acoustic modes. This phenomenon is similar to that observed with isotope doping in in-plane graphene structures.

We also unveiled that the behavior of the variation of the thermal conductance with the twisted angle is associated directly with the overlap area between the twisted and non-twisted layers.

The magnitude of the critical angles relies on the size of the nanofibers, and in particular, on the relative ratio between the widths along the zigzag and armchair edges of the nanofibers, thus demonstrating the dominance of the finite-size effect in the variation of the thermal conductance of a twisted graphite nanofiber.

Finally, we also pointed out that the correlation between the overlap area and the thermal conductance is much weaker and almost negligible in the case of circular cross-section nanofibers due to the small variation of the overlap area as a function of the twisted angle.

Our findings provide fundamental understanding of the thermal transport in twisted-layer graphite nanofibers and also point out potential applications of this effect in areas such as thermoelectrics.

Acknowledgments

This work was supported by the French National Research Agency via the Placho project grant (ANR-21-CE50-0008). Thanh-Tra Vu also acknowledges the funding by Vietnam National Foundation for Science and Technology Development (NAFOSTED) under grant number 103.01-2018.338

References

- [1] J.M.B. Lopes dos Santos, N.M.R. Peres, A.H. Castro Neto, Graphene Bilayer with a Twist: Electronic Structure, *Phys. Rev. Lett.* 99 (2007) 256802. <https://doi.org/10.1103/PhysRevLett.99.256802>.
- [2] J. Hass, F. Varchon, J.E. Millán-Otoya, M. Sprinkle, N. Sharma, W.A. De Heer, C. Berger, P.N. First, L. Magaud, E.H. Conrad, Why multilayer graphene on 4H-SiC(0001) behaves like a single sheet of graphene, *Phys. Rev. Lett.* 100 (2008) 125504. <https://doi.org/10.1103/PhysRevLett.100.125504>.
- [3] P. Poncharal, A. Ayari, T. Michel, J.-L. Sauvajol, Raman spectra of misoriented bilayer graphene, *Phys. Rev. B.* 78 (2008) 113407. <https://doi.org/10.1103/PhysRevB.78.113407>.
- [4] S. Shallcross, S. Sharma, O.A. Pankratov, Quantum Interference at the Twist Boundary in Graphene, *Phys. Rev. Lett.* 101 (2008) 056803.

- <https://doi.org/10.1103/PhysRevLett.101.056803>.
- [5] R. Bistritzer, A.H. MacDonald, Moiré bands in twisted double-layer graphene, *Proc. Natl. Acad. Sci. U. S. A.* 108 (2011) 12233–12237. <https://doi.org/10.1073/pnas.1108174108>.
- [6] Y. Cao, V. Fatemi, S. Fang, K. Watanabe, T. Taniguchi, E. Kaxiras, P. Jarillo-Herrero, Unconventional superconductivity in magic-angle graphene superlattices, *Nature*. 556 (2018) 43–50. <https://doi.org/10.1038/nature26160>.
- [7] F. Haddadi, Q.S. Wu, A.J. Kruchkov, O. V. Yazyev, Moiré Flat Bands in Twisted Double Bilayer Graphene, *Nano Lett.* 20 (2020) 2410–2415. <https://doi.org/10.1021/acs.nanolett.9b05117>.
- [8] G. Tarnopolsky, A.J. Kruchkov, A. Vishwanath, Origin of Magic Angles in Twisted Bilayer Graphene, *Phys. Rev. Lett.* 122 (2019) 106405. <https://doi.org/10.1103/PhysRevLett.122.106405>.
- [9] M. Yankowitz, S. Chen, H. Polshyn, Y. Zhang, K. Watanabe, T. Taniguchi, D. Graf, A.F. Young, C.R. Dean, Tuning superconductivity in twisted bilayer graphene, *Science* (80-.). 363 (2019) 1059–1064. <https://doi.org/10.1126/science.aav1910>.
- [10] X. Liu, Z. Wang, K. Watanabe, T. Taniguchi, O. Vafek, J.I.A. Li, Tuning electron correlation in magic-angle twisted bilayer graphene using Coulomb screening, *Science* (80-.). 371 (2021) 1261–1265. <https://doi.org/10.1126/science.abb8754>.
- [11] B.L. Chittari, N. Leconte, S. Javvaji, J. Jung, Pressure induced compression of flatbands in twisted bilayer graphene, *Electron. Struct.* 1 (2018) 015001. <https://doi.org/10.1088/2516-1075/aaead3>.
- [12] A. Fischer, Z.A.H. Goodwin, A.A. Mostofi, J. Lischner, D.M. Kennes, L. Klebl, Unconventional superconductivity in magic-angle twisted trilayer graphene, *Npj Quantum Mater.* 7 (2022) 5. <https://doi.org/10.1038/s41535-021-00410-w>.
- [13] P. Kang, W. Zhang, V. Michaud-Rioux, X. Wang, J. Yun, H. Guo, Twistronics in tensile strained bilayer black phosphorus, *Nanoscale*. 12 (2020) 12909–12916. <https://doi.org/10.1039/d0nr02179b>.
- [14] Z. Hennighausen, S. Kar, Twistronics: a turning point in 2D quantum materials, *Electron. Struct.* 3 (2021) 014004. <https://doi.org/10.1088/2516-1075/abd957>.

- [15] M.-H. Wang, Y.-E. Xie, Y.-P. Chen, Thermal transport in twisted few-layer graphene, *Chinese Phys. B.* 26 (2017) 116503. <https://doi.org/10.1088/1674-1056/26/11/116503>.
- [16] X. Nie, L. Zhao, S. Deng, Y. Zhang, Z. Du, How interlayer twist angles affect in-plane and cross-plane thermal conduction of multilayer graphene: A non-equilibrium molecular dynamics study, *Int. J. Heat Mass Transf.* 137 (2019) 161–173. <https://doi.org/10.1016/j.ijheatmasstransfer.2019.03.130>.
- [17] A.I. Cocemasov, D.L. Nika, A.A. Balandin, Phonons in twisted bilayer graphene, *Phys. Rev. B.* 88 (2013) 035428. <https://doi.org/10.1103/PhysRevB.88.035428>.
- [18] D.L. Nika, A.I. Cocemasov, A.A. Balandin, Specific heat of twisted bilayer graphene: Engineering phonons by atomic plane rotations, *Appl. Phys. Lett.* 105 (2014) 031904. <https://doi.org/10.1063/1.4890622>.
- [19] S. Han, X. Nie, S. Gu, W. Liu, L. Chen, H. Ying, L. Wang, Z. Cheng, L. Zhao, S. Chen, Twist-angle-dependent thermal conduction in single-crystalline bilayer graphene, *Appl. Phys. Lett.* 118 (2021) 193104. <https://doi.org/10.1063/5.0045386>.
- [20] K. Nakada, M. Fujita, G. Dresselhaus, M.S. Dresselhaus, Edge state in graphene ribbons: Nanometer size effect and edge shape dependence., *Phys. Rev. B.* 54 (1996) 17954–17961. <https://doi.org/10.1103/PhysRevB.54.17954>.
- [21] Y.W. Son, M.L. Cohen, S.G. Louie, Energy gaps in graphene nanoribbons, *Phys. Rev. Lett.* 97 (2006) 216803. <https://doi.org/10.1103/PhysRevLett.97.216803>.
- [22] K. Wakabayashi, K. Sasaki, T. Nakanishi, T. Enoki, Electronic states of graphene nanoribbons and analytical solutions, *Sci. Technol. Adv. Mater.* 11 (2010) 054504. <https://doi.org/10.1088/1468-6996/11/5/054504>.
- [23] V.-T. Tran, J. Saint-Martin, P. Dollfus, S. Volz, High thermoelectric performance of graphite nanofibers, *Nanoscale.* 10 (2018) 3784–3791. <https://doi.org/10.1039/C7NR07817J>.
- [24] A. Chambers, C. Park, R.T.K. Baker, N.M. Rodriguez, Hydrogen storage in graphite nanofibers, *J. Phys. Chem. B.* 102 (1998) 4253–4256. <https://doi.org/10.1021/jp980114l>.
- [25] R.D. Weinstein, T.C. Kopec, A.S. Fleischer, E. D’Addio, C. a. Bessel, The Experimental Exploration of Embedding Phase Change Materials With Graphite Nanofibers for the Thermal Management of Electronics, *J. Heat Transfer.* 130 (2008) 042405. <https://doi.org/10.1115/1.2818764>.

- [26] A. Kimouche, M.M. Ervasti, R. Drost, S. Halonen, A. Harju, P.M. Joensuu, J. Sainio, P. Liljeroth, Ultra-narrow metallic armchair graphene nanoribbons, *Nat. Commun.* 6 (2015) 10177. <https://doi.org/10.1038/ncomms10177>.
- [27] L. Wirtz, A. Rubio, The phonon dispersion of graphite revisited, *Solid State Commun.* 131 (2004) 141–152. <https://doi.org/10.1016/j.ssc.2004.04.042>.
- [28] V.-T. Tran, J. Saint-Martin, P. Dollfus, High thermoelectric performance in graphene nanoribbons by graphene/BN interface engineering, *Nanotechnology.* 26 (2015) 495202. <https://doi.org/10.1088/0957-4484/26/49/495202>.
- [29] R. Saito, G. Dresselhaus, M.S.D. Dresselhaus, A. Jorio, R. Saito, G. Dresselhaus, M.S.D. Dresselhaus, A. Jorio, *Physical Properties of Carbon Nanotubes*, Imperial College Press, 1998. <https://doi.org/10.1063/1.56490>.
- [30] S. Datta, Nanoscale device modeling: the Green's function method, *Superlattices Microstruct.* 28 (2000) 253–278. <https://doi.org/10.1006/spmi.2000.0920>.
- [31] Y. Wu, P.A. Childs, Conductance of Graphene Nanoribbon Junctions and the Tight Binding Model, *Nanoscale Res. Lett.* 6 (2011) 1–5. <https://doi.org/10.1007/s11671-010-9791-y>.
- [32] C.H. Lewenkopf, E.R. Mucciolo, The recursive Green's function method for graphene, *J. Comput. Electron.* 12 (2013) 203–231. <https://doi.org/10.1007/s10825-013-0458-7>.
- [33] C. Pickard, M. Payne, Extrapolative approaches to Brillouin-zone integration, *Phys. Rev. B.* 59 (1999) 4685–4693. <https://doi.org/10.1103/PhysRevB.59.4685>.
- [34] V.-T.T. Tran, J. Saint-Martin, P. Dollfus, S. Volz, High thermoelectric and electronic performance in graphene nanoribbons by isotope and vacancy engineering, *Mater. Today Proc.* 5 (2018) 10393–10400. <https://doi.org/10.1016/j.matpr.2017.12.287>.
- [35] R.M. Jacobberger, B. Kiraly, M. Fortin-Deschenes, P.L. Levesque, K.M. McElhinny, G.J. Brady, R. Rojas Delgado, S. Singha Roy, A. Mannix, M.G. Lagally, P.G. Evans, P. Desjardins, R. Martel, M.C. Hersam, N.P. Guisinger, M.S. Arnold, Direct oriented growth of armchair graphene nanoribbons on germanium., *Nat. Commun.* 6 (2015) 8006. <https://doi.org/10.1038/ncomms9006>.
- [36] A. Kimouche, M.M. Ervasti, R. Drost, S. Halonen, A. Harju, P.M. Joensuu, J. Sainio, P. Liljeroth, Ultra-narrow metallic armchair graphene nanoribbons, *Nat. Commun.* 6 (2015) 10177. <https://doi.org/10.1038/ncomms10177>.

- [37] R.L. Poveda, N. Gupta, *Carbon Nanofiber Reinforced Polymer Composites*, Springer International Publishing, 2015. <https://doi.org/10.1007/978-3-319-23787-9>.
- [38] G.G. Tibbetts, M.L. Lake, K.L. Strong, B.P. Rice, A review of the fabrication and properties of vapor-grown carbon nanofiber/polymer composites, *Compos. Sci. Technol.* 67 (2007) 1709–1718. <https://doi.org/10.1016/j.compscitech.2006.06.015>.
- [39] M.H. Al-Saleh, U. Sundararaj, A review of vapor grown carbon nanofiber/polymer conductive composites, *Carbon* N. Y. 47 (2009) 2–22. <https://doi.org/10.1016/j.carbon.2008.09.039>.
- [40] M. Liao, Z. Wei, L. Du, Q. Wang, J. Tang, H. Yu, F. Wu, J. Zhao, X. Xu, B. Han, K. Liu, P. Gao, T. Polcar, Z. Sun, D. Shi, R. Yang, G. Zhang, Precise control of the interlayer twist angle in large scale MoS₂ homostructures, *Nat. Commun.* 11 (2020) 2153. <https://doi.org/10.1038/s41467-020-16056-4>.
- [41] C. Yu, S. Saha, J. Zhou, L. Shi, A.M. Cassell, B.A. Cruden, Q. Ngo, J. Li, Thermal contact resistance and thermal conductivity of a carbon nanofiber, *J. Heat Transfer.* 128 (2006) 234–239. <https://doi.org/10.1115/1.2150833>.
- [42] E. Mayhew, V. Prakash, Thermal conductivity of individual carbon nanofibers, *Carbon* N. Y. 62 (2013) 493–500. <https://doi.org/10.1016/j.carbon.2013.06.048>.